




Ultralight, superelastic pure graphene aerogel for piezoresistive sensing application

Gaochuang Yang^{1,2}, Xiaoli Qin³, Tiandi Chen¹, Jinqing Wang^{1,2,*} , Limin Ma^{1,2}, and Shengrong Yang^{1,2,*}

¹ State Key Laboratory of Solid Lubrication, Lanzhou Institute of Chemical Physics, Chinese Academy of Sciences, Lanzhou 730000, China

² Center of Materials Science and Optoelectronics Engineering, University of Chinese Academy of Sciences, Beijing 100049, China

³ School of Stomatology, Lanzhou University, Lanzhou 730000, China

Received: 30 July 2022

Accepted: 20 December 2022

Published online:
4 January 2023

© The Author(s), under exclusive licence to Springer Science+Business Media, LLC, part of Springer Nature 2023

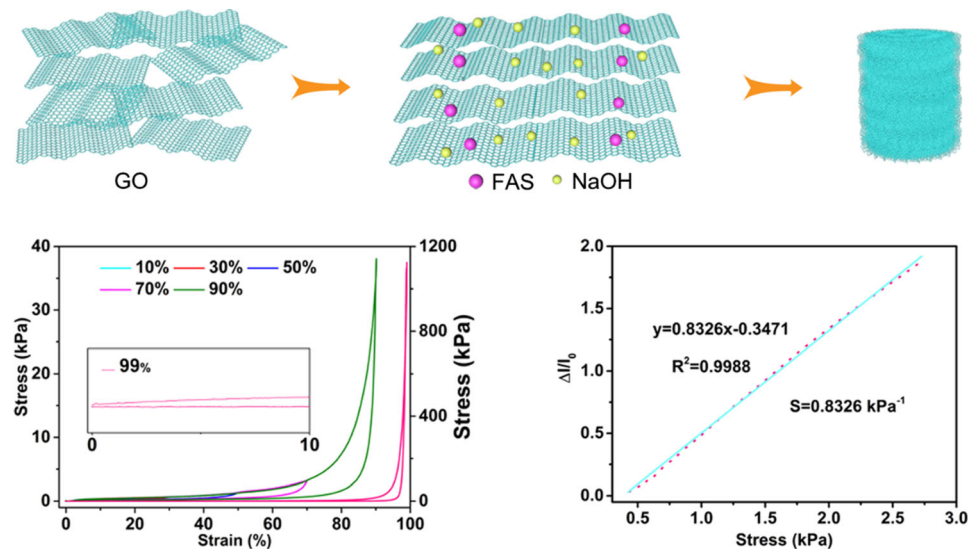
ABSTRACT

Graphene aerogel (GA), with low density, high conductivity, and good mechanical properties, has important application potentials in the field of flexible electronics. Here, a balanced approach was developed in this work: Graphene oxide (GO) nanosheets were induced to assemble into a homogeneous porous hydrogel under alkali induction, and then, the oxygen-containing functional groups of GO were removed by reductant of formamidine sulfonic acid (FAS). Besides, the hydrogel of GA precursor can be quickly dried at a high temperature (150 °C) within 30 min to obtain pure GA of FGA. After further calcination, the obtained aerogel of AFGA with ordered structure has ultralow density (3.88 mg/cm³), high conductivity (7.4 S/m), supercompression recovery performance (99%), high sensitivity ($S = 0.83 \text{ kPa}^{-1}$), large reversible compression cycle performance (200 cycles under 90% strain), and high fatigue resistance (10,000 cycles under 70% strain), which presents excellent piezoresistive properties and can find wide applications in piezoresistive sensors as the high-performance sensing material.

Handling Editor: Mark Bissett.

Address correspondence to E-mail: jqwang@licp.cas.cn; sryang@licp.cas.cn

GRAPHICAL ABSTRACT



Introduction

In recent years, the development and application of flexible sensors make people's quality of life improve greatly, providing significant convenience in many aspects [1–6]. Aerogel has been widely used in energy storage, environmental protection, electromagnetic shielding, and other fields because of its unique properties, such as high porosity, high specific surface area, and low density [7–11]. More importantly, since conductive aerogel can convert its mechanical deformation into electrical output signals, it has attracted great attention in flexible sensor applications, such as wearable pressure-sensitive electronic devices, electronic skins, and artificial intelligence [12–16]. In particular, there have been many reports using various nanomaterials represented by graphene to prepare macroscopic aerogel [17, 18]. As an important derivative of graphene, graphene oxide (GO) not only inherits the structural characters and unique properties of graphene but also has good water solubility and easy assembly due to its rich functional groups, which is especially suitable for preparing ultralight and elastic graphene aerogel (GA) for assembling flexible piezoresistive sensors [19, 20].

GA is usually prepared by two basic approaches: the ice-templating method and the sol-gel method [21, 22]. Although exhibiting high designability in structure and function, the ice-templating method inevitably adopts the freeze-drying process to remove the template. However, the freeze-drying process of GA tends to be time-consuming (generally more than 72 h), limiting the quick and large-scale production of GA [23]. With the hydrothermal reaction or reducing agents, such as hydrazine hydrate, ethylenediamine, and ascorbic acid, the sol-gel method uses chemical reduction technology to achieve cross-linking among thin sheets and chemical transformation inside the thin sheets to generate a three-dimensional (3D) network structure [14, 24–27]. However, the high-temperature and high-pressure treatments in the hydrothermal reaction are very dangerous, and commonly used reductants are either toxic, flammable, expensive, or hard to be removed [28–30]. Thus, it is crucial to find a suitable reductant for substitution and improvement of reduction quality. Furthermore, GO's varying size, easy stacking, and inconclusive distribution of oxygen-containing groups are huge obstacles to accurately organizing its nanosheets into an ordered 3D structure. Fortunately, Yao et al. [31] demonstrated that alkali could induce GO liquid crystals (GO LCs) to

form a highly ordered structure, endowing graphene sheets with a long-range ordered microstructure in the 3D framework.

Here, a balanced method was developed to prepare GA: GO nanosheets were assembled into 3D ordered structure with alkali induction and subsequently in situ reduced using an industrial reductant of formamidine sulfinic acid (FAS). FAS exhibits the following advantages as an efficient reductant: (1) environmental friendliness and (2) safe and cost-effective for bulk production. What is more, the GA obtained by FAS reduction (named FGA) can be directly dried at a high temperature (150 °C) rapidly (within 30 min) without noticeable shrinkage, different from gels obtained by other reducing agents. Then, the FGA was further annealed (named AFGA) and applied for the following testing. The prepared AFGA has ultralow density (3.88 mg/cm³), high conductivity (7.4 S/m), supercompression recovery performance (99%), high sensitivity ($S = 0.83 \text{ kPa}^{-1}$), enormous reversible compression cycle performance (200 cycles under 90% strain), and high fatigue resistance (10000 cycles under 70% strain), which can find wide applications in piezoresistive sensors.

Experimental method

Materials

Formamidine sulfinic acid (FAS, 98%) was purchased from Shanghai Xianding Biotechnology Co., Ltd. NaOH and KOH with 99% purity were purchased from Lian-Long Bohua (Tianjin) Pharmaceutical and Chemical Co., Ltd. Graphite powder (325 mesh, 99.9%) was purchased from Qingdao Huatai Lubrication Sealing Technology Co., Ltd. Deionized water (> 18 M Ω -cm) is homemade and used throughout for preparation and washing.

Preparation of aerogel

GO was prepared from natural graphite powder based on our previous work [32]. Firstly, a FAS alkali solution was prepared, in which the concentrations of the FAS and NaOH were set as 0.5 and 2.67 M, respectively. Then, the FAS alkali solution was added to the prepared GO solution, and the GO and alkali concentrations were adjusted to 5 mg/mL and 0.16 M. After that, the evenly mixed solution was

reacted at 90 °C for 2 h to form a hydrogel, which was subsequently removed and cooled to room temperature. The hydrogel was frozen in a refrigerator for 5 h, then thawed, and further reacted for 8 h. After being dialyzed with water and ethanol for 24 h, the gel was dried at 150 °C and further annealed at 500 °C to generate FGA and AFGA, respectively.

Preparations of sensor and array

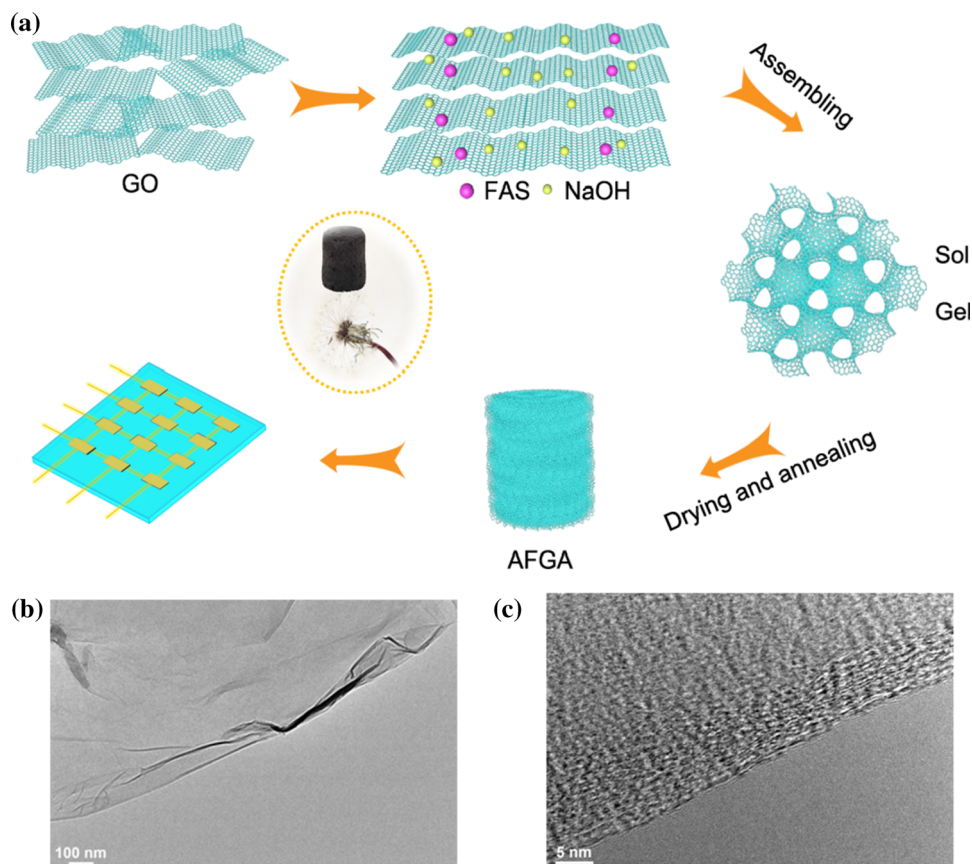
Sensor preparation: Firstly, a mechanical cutting device was used to cut the optimum AFGA aerogel into slices with a radius of 0.8 cm and a thickness of approximately 0.2 cm. Then, the silver paste was used to connect the two copper wires to the upper and lower sides of the aerogel silice to establish external contact. Finally, the sensor was encapsulated with medical tape.

Array preparation: Firstly, the optimum AFGA aerogel was cut into 12 small rectangles with a length of 0.8 cm and a width of 0.4 cm, which were then fixed one by one according to the position of the array plate; finally, they were encapsulated by a transparent polyester film.

Characterizations

The morphology and size of GO nanosheets were photographed by transmission electron microscope (TEM, TF20) and atomic force microscope (AFM, Bruker-Veeco). X-ray photoelectron spectroscopy (XPS) was measured by an X-ray photoelectron spectrometer using monochromatic Al-K α radiation as an excitation source on ESCALab MKII. X-ray diffraction (XRD) pattern was obtained by a diffractometer (Bruker D8 Advance, Germany) with an operating current of 40 mA, and a voltage of 40 kV. Raman spectroscopy was performed using HORIBA Jobin Yvon (S.A.S.). The mechanical performances of the AFGA aerogels were measured using an AGS-X universal testing machine. All the resistance and current signals were recorded using a Keithley 2450 Multimeter in voltage scanning mode.

Figure 1 **a** Schematic diagram on the preparation of the AFGA aerogel. **b** TEM and **c** HRTEM images of GO nanosheets.



Results and discussion

Structural characterizations

As depicted in Fig. 1a, the preparation process of aerogels mainly involves three key steps: sol-gel, reduction, and drying processes. Figure 1b, c provides TEM images of the prepared high-quality GO nanosheets. The thickness of the GO nanosheet was determined by AFM analysis, which indicated that its thickness was less than 1 nm, corresponding to two or three stacked layers (Fig. S1, Supporting Information). XRD analysis was further carried out to confirm the crystal structure of the sample, and a strong (001) diffraction peak near 10.65° can be clearly observed, which is a typical peak of GO (Fig. 3a) [33]. Next, alkali (NaOH) induction and chemical reduction were performed at a mild temperature (90°C) to form graphene hydrogel, where the GO solution is transformed from the sol into the gel. As illustrated in Scheme S1, FAS is easily decomposed in an alkaline solution to generate sulfites, which could remove GO's oxygen-containing groups ($-\text{OH}$, $\text{C}-\text{O}-\text{C}$, $\text{C}=\text{O}$) [34]. During the formation of hydrogel, the alkali

concentration has the most significant impact on the final shape of the aerogel. It was observed through polarized light optical microscope (POM) images that GO could form a well-organized texture structure under the induction of alkali solution (Fig. S2a), while the pure GO suspension showed a disordered phase at the same concentration (Fig. S2b) [31].

Furthermore, the integrity of aerogel can be adjusted by the alkali content (Table S1). Series of AFGA samples were synthesized at different alkali concentrations (0.12, 0.14, 0.16, 0.18, 0.20, and 0.22 M) and named as AFGA-0, AFGA-1, AFGA-2, AFGA-3, AFGA-4, and AFGA-5, respectively. Different alkali concentrations led to different shrinkage degrees of AFGA (Fig. S3). When GO was induced at a low alkali concentration (0.12 M), AFGA-0 seriously shrank, and AFGA-0 obtained even by freeze-drying also underwent severe shrinkage (Fig. S4). AFGA-1 at the alkali concentration of 0.14 M showed a relatively complete appearance, but it was not pressure-resistant and easily broken after 5 gentle finger compressions. AFGA-2 at the alkali concentration of 0.16 M could be recovered as before after compression

(Fig. S5). When the alkali concentration increases to 0.18 M and above, there will also be significant shrinkage, but it will not collapse (Fig. S3). Therefore, appropriate alkali concentration is pretty crucial for the final appearance and performance of GA. By replacing the alkali of NaOH with KOH, the influence of different metal ions on the formation of AFGA is explored, and the as-prepared AFGA exhibits more evident shrinkage (Fig. S6), which may be caused by the larger hydrated radius of K^+ than Na^+ . Namely, the larger the radius is, the less the electric double-layer charges of colloidal GO sheets will be neutralized, which would lead to the failure to induce the assembly of GO nanosheets [31].

The internal pore structure of the aerogel plays an essential role in its properties. After being reduced to form a stable hydrogel, it is removed and placed on a cold source for freezing to form ice crystals. Ice crystals are used to create directional pore diameters inside the hydrogel, which is a general method to produce a 3D porous structure [35]. Wicklein et al. [36] reported that a higher freezing rate resulted in smaller pore diameter, and the directional freezing was conducted using a $-20\text{ }^\circ\text{C}$ cold source to form a hydrogel with a larger internal pore size. Next, drying the prepared hydrogel is necessary for manufacturing GA, and it is imperative to adopt a suitable drying method. GA usually suffers from volume shrinkage and structural damage caused by temperature and pressure during drying. According to Laplace's formula ($P_c = (-2\gamma \times \cos(\theta))/r$), capillary pressure (P_c) is defined as the functions of the solvent surface tension (γ), contact angle (θ), and pore radius (r) [26]. It can be obtained from this equation that the capillary pressure is reduced by adjusting the solvent surface tension, contact angle, and pore radius. Considering the reduction of the hydrogel and the larger pore size caused by freezing, the capillary pressure is reduced by dropping the surface tension. According to the Aspen simulated physical property data analysis, from room temperature to $200\text{ }^\circ\text{C}$, the surface tension of water is higher than that of ethanol (Fig. S7) [37]. Using ethanol instead of water for dialysis can effectively reduce the surface tension and then dry at $150\text{ }^\circ\text{C}$ to quickly obtain the FAS-reduced aerogel.

FGA was obtained by drying GA precursor at different temperatures of 25, 60, 90, 120, 150, and $180\text{ }^\circ\text{C}$. It was evident that partial shrinkage occurred at temperatures lower than $120\text{ }^\circ\text{C}$, while relatively

complete FGA could be obtained only at high temperatures of 150 and $180\text{ }^\circ\text{C}$ (Fig. S8). By comparing its density with freeze-drying (FD), drying at $150\text{ }^\circ\text{C}$ shrinks only by 7%, and its density is only 3.88 mg/cm^3 (Fig. S9). Although freeze-drying can achieve a smaller density, it will lead to larger cracks and holes in its appearance, which is far less complete and robust than that drying at $150\text{ }^\circ\text{C}$ (Fig. S10). In addition, since a higher drying temperature will lead to a faster drying speed, the drying time at $150\text{ }^\circ\text{C}$ is less than 30 min. Compared with other drying methods, high-temperature rapid drying presents apparent advantages (Table S2). Finally, the impurities are further removed by annealing at $500\text{ }^\circ\text{C}$ to obtain the annealed FGA (AFGA).

The internal structure of AFGA-2 was observed by SEM. As shown in Fig. 2a, b, AFGA-2 exhibits a stable porous structure due to its composition of interconnected reduced GO (rGO) sheets partially overlapping in a 3D configuration through π - π interactions to form a solid honeycomb structure. In addition, an ordered honeycomb structure of AFGA-2 avoids the volume shrinkage [38]. Obviously, the walls of the aerogel are mainly composed of bilayer or multilayer graphene sheets, which dramatically enhances the structural stability of the aerogel (Fig. 2c, d). As shown in Fig. 2e, the internal pore appearance of AFGA-2 is similar to a circular ring, with a pore size of approximately $70\text{ }\mu\text{m}$ (Fig. S11) [39]. Energy-dispersive X-ray (EDX) elemental analysis indicates that the prepared AFGA only contains two elements of C and O (Fig. S12), confirming that the prepared AFGA is pure and does not contain other impurities. As shown in Fig. 2f, the magnified cell walls of AFGA-2 are full of folds, which may be caused by the disappearance of a large number of functional groups after the reduction of GO. The reduced surface energy through GO's mutual reaction and recombination lead to the structural transformation from 2 to 3D, thus resulting in the wrinkled surface of the textures [40, 41]. Chen et al. [42] believed that wrinkles/folds would make rGO achieve hydrophobic performance, which was confirmed by measuring its water contact angle (WCA). WCA values of AFGA samples with different alkali concentrations are all greater than 100° , and the maximum value of AFGA-2 is 126.4° (Fig. S13) [43]. Observing the internal structures of AFGA-1, AFGA-3, AFGA-4, and AFGA-5 by SEM, it can be clearly obtained that alkali concentration has a tremendous

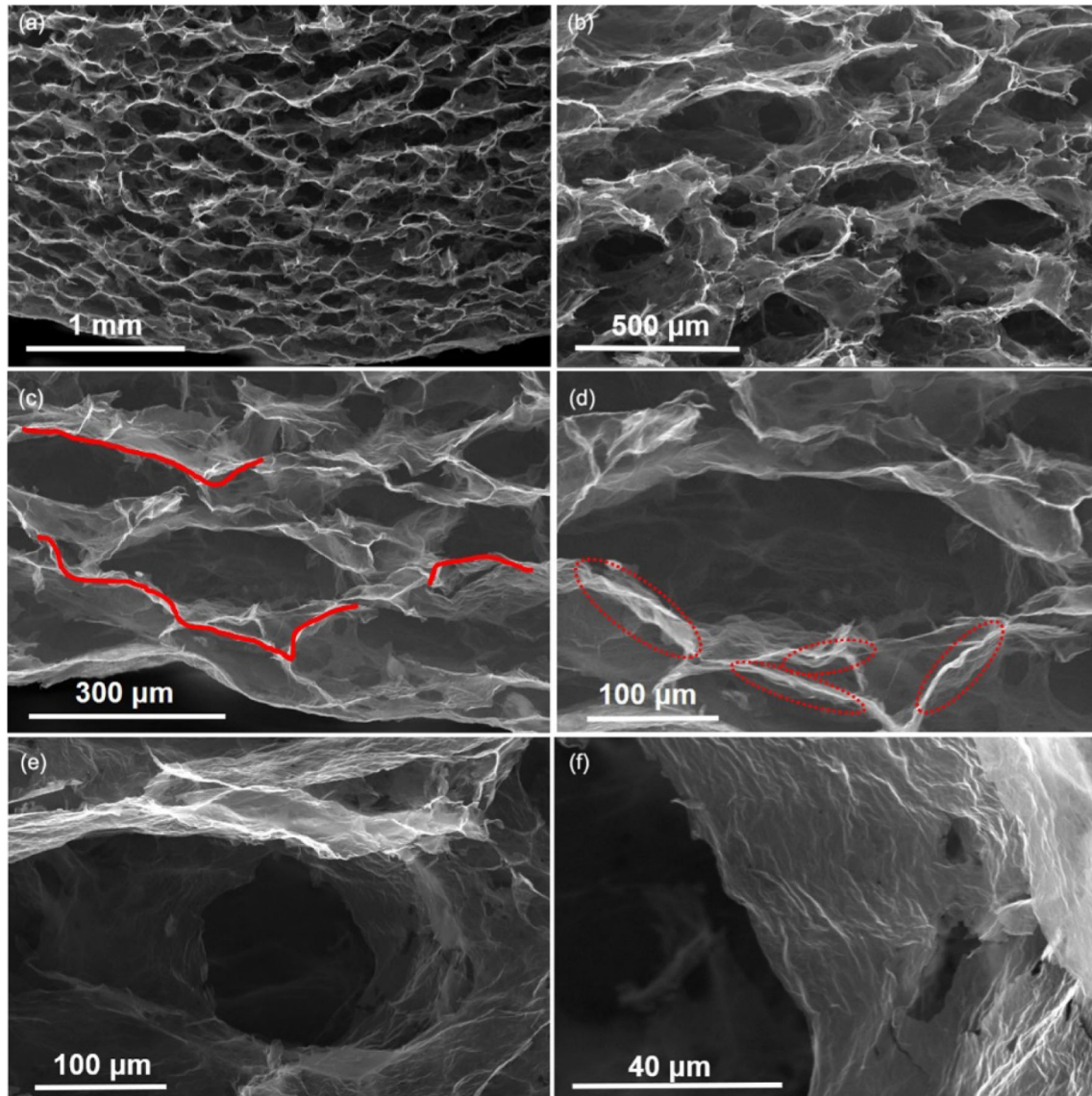


Figure 2 a–f SEM images of the AFGA-2 composite aerogel at different magnifications.

influence on the internal system of AFGA (Fig. S14). The AFGA-1 interior is similar to a stack of pieces with only a few voids, which may cause its fragility. Small and disordered internal pores will appear when the alkali concentration is further increased (> 1.6 M), which is the leading cause of volume shrinkage. In conclusion, proper alkali concentration induction is essential for forming GA with proper nanostructures and performances.

Figure 3a shows XRD patterns of GO, FGA, and AFGA. FGA presents a weak and broad (002) diffraction peak at $2\theta = 24.05^\circ$, corresponding to a d-spacing of approximately 0.370 nm. After annealing, AFGA showed relatively sharp (002) diffraction

peak at $2\theta = 25.35^\circ$, corresponding to the d-spacing decreasing to 0.351 nm. These results approved the successful reduction of GO by FAS and the further quality improvement of rGO after annealing. Raman scattering is very sensitive to electronic structure and can be used to characterize graphene materials effectively. As shown in Fig. 3b, the G-band of GO was near 1587 cm^{-1} , while the D-band appeared in a lower region of 1346 cm^{-1} , indicating that the characteristics structure of sp^2 is damaged because more defects and a large number of oxidation sites are generated on the sheet. Among them, the strength ratio of the D-band to the G-band (I_D/I_G) is approximately 0.93 [44]. Upon the reduction of FAS and

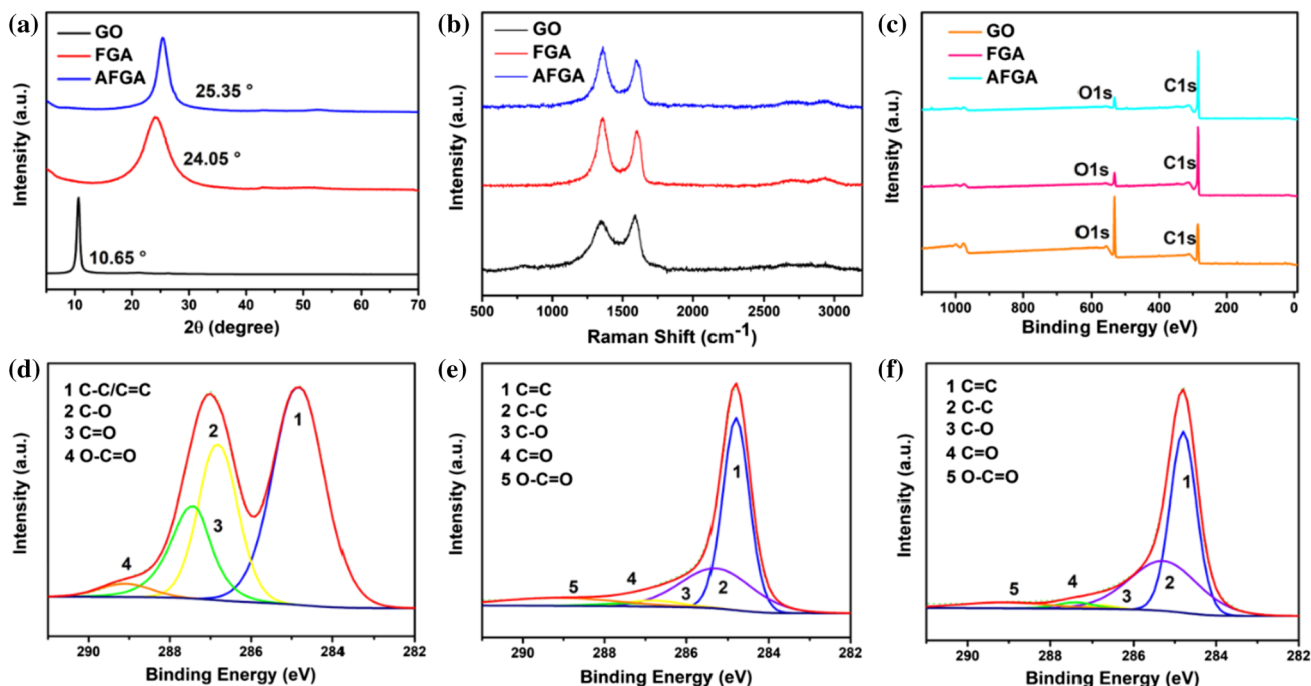


Figure 3 **a** XRD patterns, **b** Raman spectra, and **c** XPS survey spectra of GO, FGA, and AFGA. **d–f** High-resolution XPS spectra of C1s for GO, FGA, and AFGA.

further annealing, I_D/I_G increased significantly, reaching 1.19, attributable to the removal of many oxygen-containing functional groups during the reduction process and the formation of smaller and more graphene domains [45, 46].

XPS characterization was further performed to analyze the GO's reduction degree by FAS. Apparent changes of the C peak and O peak in Fig. 3c prove that the reduction of FAS and further annealing remove GO's oxygen-containing groups. For GO, the peak intensity of O 1s was significantly higher than that of C 1s. After reduction, the peak intensity of C 1s of FGA and AFGA was significantly higher than that of O 1s. As shown in Fig. 3d, GO showed some typical C 1s peaks of C=C/(C–C), C–O, C=O, and O–C=O groups at 284.8, 286.8, 287.4, and 288.7 eV, respectively [46]. Upon the reduction, both FGA and AFGA showed the related groups, and the peak intensity related to the C=C/(C–C) bond was dominant, while the intensity of the oxygen-containing groups was significantly reduced, indicating the effective removal of the oxygen-containing groups (Fig. 3e, f). The C/O atom ratio is essential evidence of GO reduction. For FGA and AFGA, the C/O atom ratios detected by XPS are 10.15 and 11.28,

respectively, which proves the strong reduction ability of the FAS agent [47]. By comparing the C/O ratios of GA reported in other literatures, AFGA has obvious advantages, as summarized in Table S2.

Electrical and mechanical properties

The electrical and mechanical properties of AFGA aerogels were measured through reasonable mechanical tests to evaluate the practicality of the prepared aerogel. As shown in Fig. 4a, compared with other alkali concentration-induced AFGA, AFGA-2 possesses the lowest density, only 3.88 mg/cm³, and its conductivity is as high as 7.4 S/m, which is attributed to its good internal arrangement structure. As shown in Fig. 4b, at 50% strain, the stress of the AFGA series increases with the density increase due to the densification of the internal structure caused by contraction. AFGA-2 achieved a modulus of 3.89 kPa, which was not much different from the AFGA-4 (4.02 kPa) with higher density, demonstrating that the ordered internal honeycomb structure is capable of effective load transfer during external compression and thus results in GA's good mechanical properties. In addition, the larger

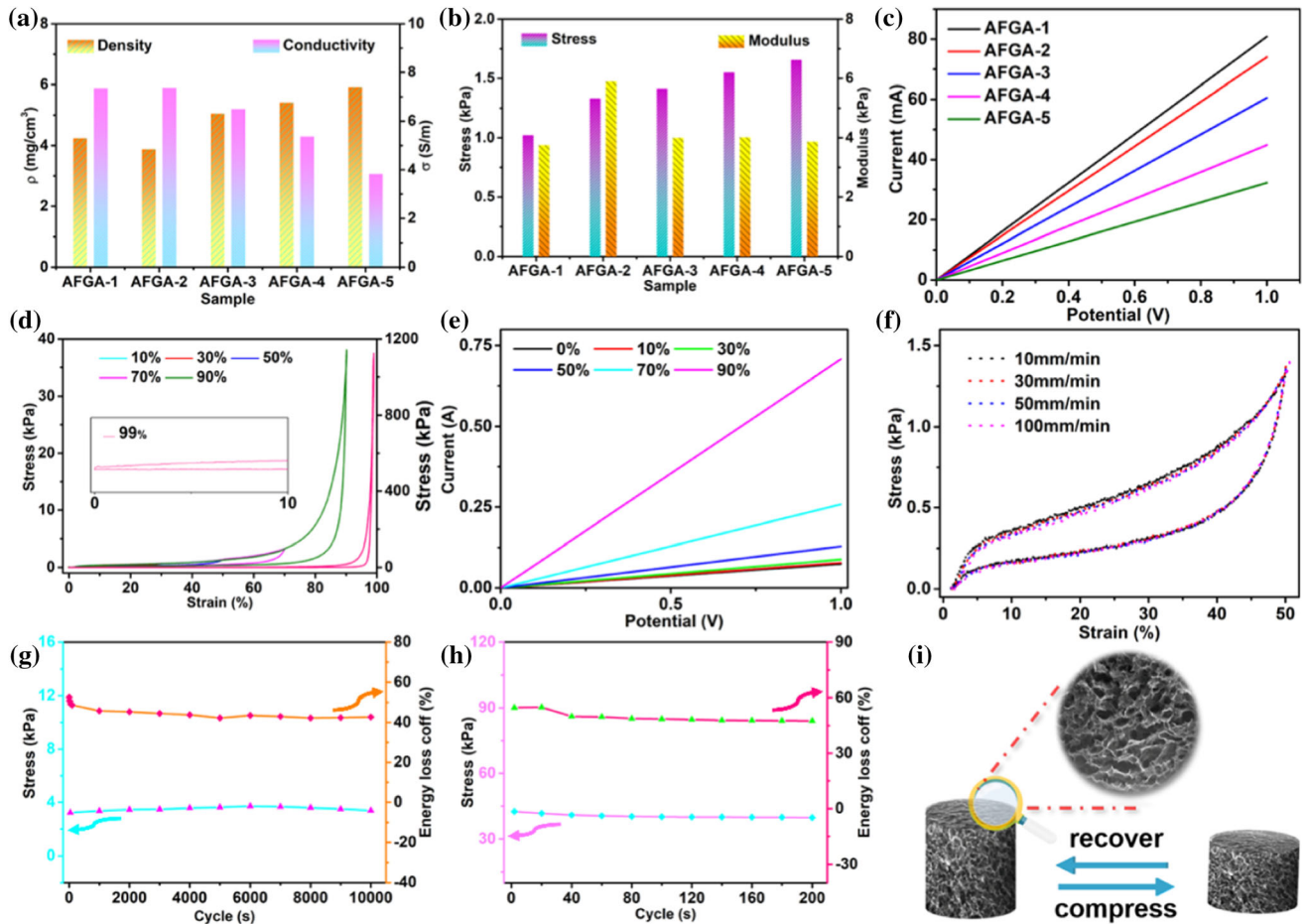


Figure 4 **a** Density and conductivity of the AFGA aerogels. **b** Compression strength and modulus of the AFGA aerogels at 50% compression strain with a compression rate of 20 mm min⁻¹. **c** *I*–*V* curves of the AFGA aerogels. **d** Typical stress–strain curves of the AFGA-2 aerogel at different set strains. **e** *I*–*V* curves of the

AFGA-2 aerogel at different set strains. **f** Stress–strain curves at different compression rates. Stress–strain and energy loss curves of the AFGA-2 aerogel **g** under 10,000 cycles at 70% strain and **h** under 200 cycles at 90% strain with a compression rate of 200 mm min⁻¹. **i** Schematic diagram of cyclic compression.

modulus could enable the AFGA aerogel framework to resist solvent evaporation capillary pressure during rapid drying at high temperatures. The *I*–*V* curve exhibited the good linear Ohmic behavior of AFGA, proving the stable electrical properties of the prepared pure GA (Fig. 4c). A series of compression tests under different strains were further carried out to evaluate the structural stability of AFGA-2, which is very important for high-performance piezoresistive sensors. As shown in Fig. 4d, AFGA-2 was compressed under the set strains. Starting from 10% strain, after 30, 50, 70, 90%, and finally 99% strain, it can completely recover after compression. In particular, when the external pressure was released under an extreme strain of 99%, it almost returned to the

original shape without visible breakage or shrinkage, and the maximum stress reached 1.12 MPa (Video S1). As summarized in Table S2, AFGA-2 has superior mechanical properties compared to other reported GA materials. Further testing of the *I*–*V* curve of AFGA-2 under different strains showed excellent linear Ohmic behavior, which would provide strong support for the fabrication of piezoresistive sensors (Fig. 4e).

Stable stress–strain curves (Fig. 4f) at different compression rates at 50% strain indicate that the compression rate does not affect the changes in its mechanical properties, which is of great significance for the practical application of piezoresistive sensors. Subsequently, 10000 cycles of compression tests were

conducted at 70% strain (Fig. 4g). Obviously, the maximum stress remained basically unchanged during the compression, while the energy loss coefficient decreased within the first 100 cycles and then maintained above 42%. Moreover, as shown in Fig. 4h, under a higher strain of 90%, the same is true for 200 cycles, maintaining high mechanical stability and a stable energy loss coefficient, proving that AFGA-2 has excellent fatigue resistance. By placing a 10 N weight on AFGA-2, it was found that AFGA-2 could support a weight more than 56000 times its own weight and could fully recover after release, demonstrating robust compressive resistance in practical applications (Fig. S15). The uniform cellular network provides inherent power and special inner structure to release the external forces and

deformations effectively, proving that GA prepared by pure GO can also possess reliable compression resilience and high strength to meet the requirements of piezoresistive sensors (Fig. 4i).

Sensing performances

The excellent mechanical strength of AFGA-2 is a prerequisite for the stability and reliability of sensors based on piezoresistive effects. Sensitivity is one of the most critical parameters for evaluating the performance of pressure sensors, and its piezoresistive sensing mechanism is depicted in Fig. 5a. As shown in Fig. 5b, the sensitivity under different pressures was tested. It exhibits linear variation ($R^2 = 0.9988$) over a wide detection range (≤ 2.72 kPa) with a high

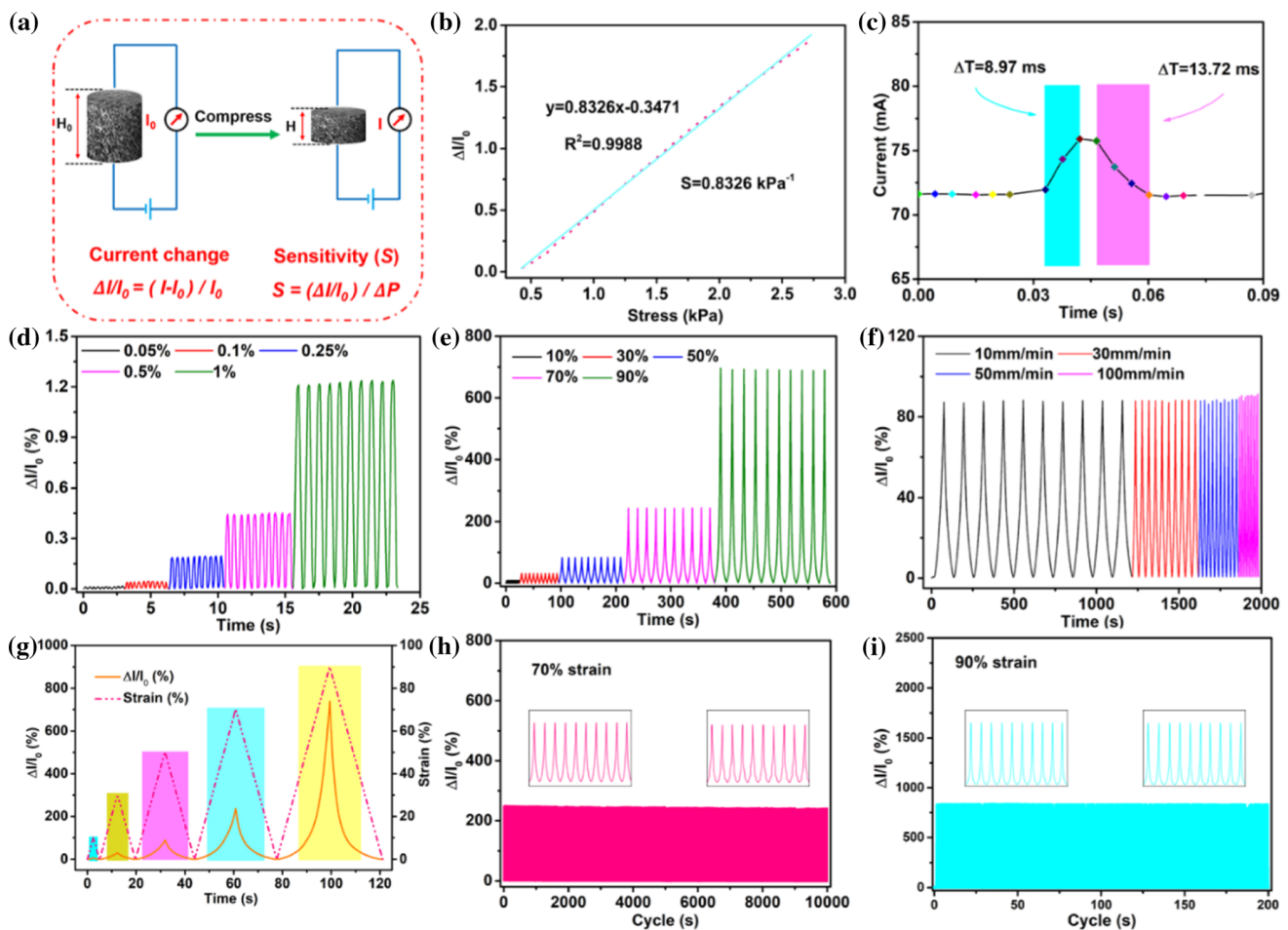


Figure 5 a Schematic diagram of aerogel sensitivity. b Sensitivity of the AFGA-2 aerogel as a function of pressure. c Response time of the fabricated AFGA-2 aerogel sensor. Cyclic piezoresistive sensing performances of the AFGA-2 aerogel under different d-e compression strain levels at a compression rate of

10 mm min⁻¹. f AFGA-2 aerogel at 50% strain with different compression rates. h Cyclic piezoresistive sensing performances of the AFGA-2 aerogel at 70% strain over 10,000 cycles and i at 90% strain over 200 cycles.

sensitivity of 0.83 kPa^{-1} , showing good pressure sensing performance attributable to the honeycomb network structure of aerogel. As another parameter of sensing performances, the response time of AFGA-2 is significant. As shown in Fig. 5c, the response time of AFGA-2 was only 8.97 ms, while its recovery time was 13.72 ms, with a minimal lag time, which is significantly better than other composite aerogels (Table S3) [23, 48, 49]. Under different pressures, the cycle stability of AFGA-2 has essential reference significance. As shown in Fig. 5d, e, AFGA-2 maintained good cyclic stability in 10 cycles at a low strain of 0.05% and showed ultralow detection limit and real-time monitoring of small changes, reflecting the excellent sensitivity of the sensor [48]. Furthermore, the AFGA-2 aerogel maintained good stability with the strain increase. As shown in Fig. 5f, the signal held a good stable direction under different compression rates, indicating that the rate does not affect the piezoresistive behavior of AFGA-2. Figure 5g presents a positive trend of strain current change from 10 to 90%, and the consistency of strain current change is detected. The cyclic stability of AFGA-2 was evaluated by performing 10,000 compression tests at a high strain of 70%, and the results are shown in Fig. 5h, where the rate of current change remained high stability. In addition, the current rate did not change significantly in the first 10 cycles or the last 10 cycles. Figure 5i shows the piezoresistive behavior at a higher strain of 90%. The change rate of current remained highly stable during 200 cycles, and no change was found by observing the beginning and the end of the cycles. As summarized in Table S3, AFGA-2 has excellent sensing performance compared with other works.

In addition, the piezoresistive ability of AFGA-2 was further tested by placing it in ethanol (Fig. S16). AFGA-2 maintained a high electrical signal and stress stability at 50% strain within 100 cycles, indicating that AFGA-2 can be used for signal transmission in some special liquids, extending its sensing application field. In addition, AFGA-2 also maintained a perfect piezoresistive effect in liquid nitrogen ($-196 \text{ }^\circ\text{C}$) and exhibited a superb signal response through using artificial compression (Fig. S17, Video S2), confirming its ultralow temperature tolerance. In short, thanks to the comprehensive properties of graphene, AFGA with excellent electrical signals has been prepared through an alkali-induced self-

assembly strategy, which provides strong support for practical sensing applications.

Sensing applications

The AFGA-based piezoresistive sensor was fabricated, and a series of tests were carried out. Figure 6a shows that the adhered sensor can continuously detect the weak characteristic peak of a volunteer's pulse. Figure 6b carried out a vibration test, and the vibration response of the mobile phone exhibited an excellent signal response law, which could provide signal support for tremors in some parts of the body. Sound detection proves the sensor's feasibility in producing speech recognition equipment. As shown in Fig. 6c, when saying "hello," the precise change in the current flowing through the sensor mirrors the change of sound. The sensor also can be applied to capture the small electrical signal generated by the face change (smiling), thus generating standard waveform output (Fig. 6d). When the sensor was fixed on the index finger joint, the finger appeared in different degrees of bending and then gradually recovered, as shown in Fig. 6e, showing good recognition of different finger bending angles. By attaching the sensor to the shoe's sole, the sensor can transmit the signal to the receiver in time through normal walking, presenting a regular response (Fig. 6f). In conclusion, the piezoresistive sensor fabricated by AFGA-2 can detect limb movements well, which is significant for wearable electronic devices and health monitoring.

Wearable pressure sensors are widely integrated into electronic skin to detect pressure distribution and the location of mechanical stimuli, and array units are often applied in the design. Here, AFGA-2 was employed to design a 3×4 array element for multipoint detection of the pressure distribution. The natural array unit and model are shown in Fig. S18a, b, and each sensor pixel was connected and assembled with a set of copper wires encapsulated by polyester film, whose working principle is depicted in Fig. 6g. Obvious resistance variation can be detected when the sugar cubes are placed at the head and tail positions (Figs. 6h, S18c, d). In addition, the array can be used to distinguish different weight signals at different positions, as shown in Fig. 6i. The number of sugar cubes in the back row was twice as much as that of the front row (Fig. S18e, f). The array can accurately sense different signals. The resistance

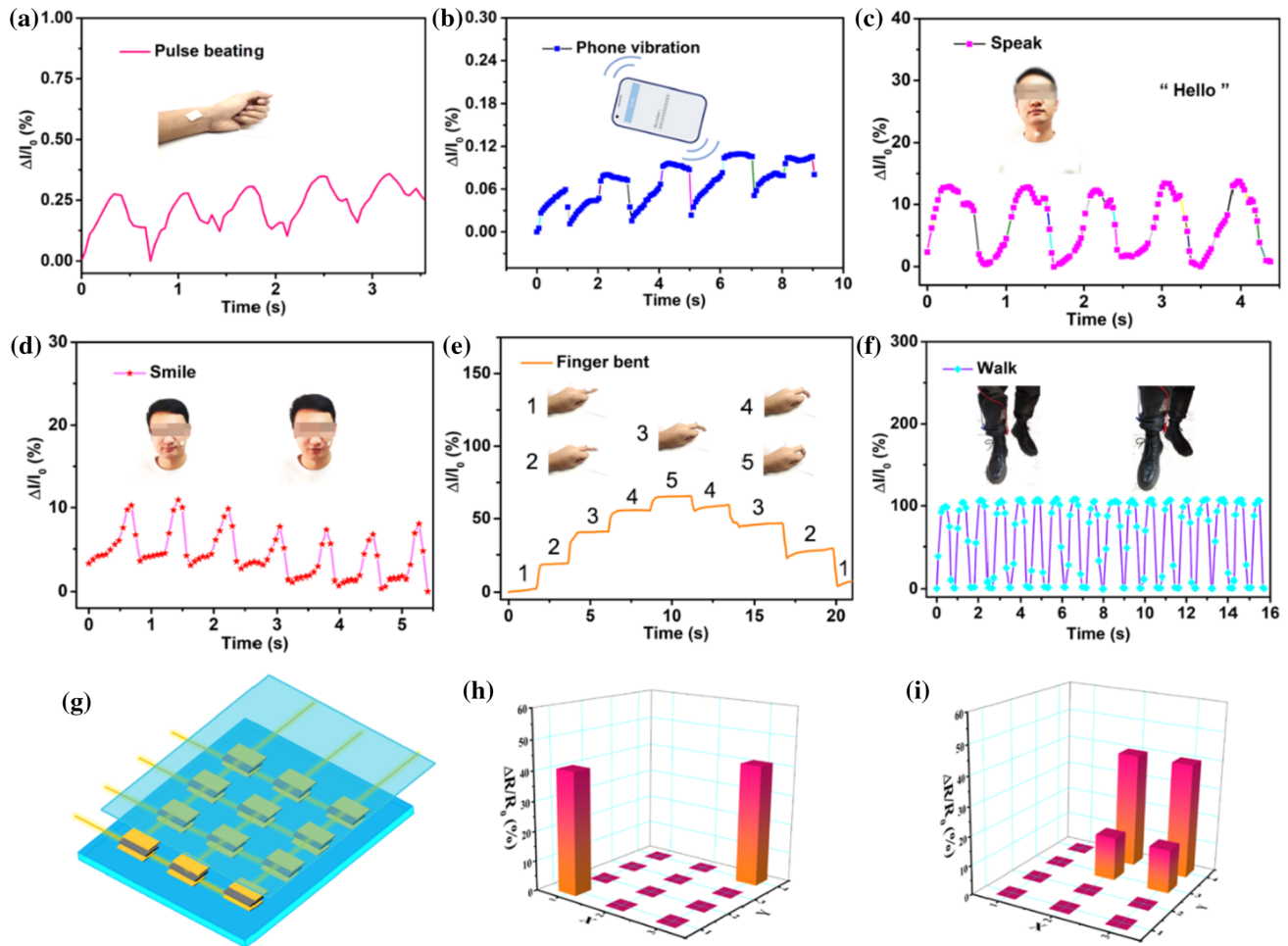


Figure 6 Sensing performances of the AFGA-2 aerogel served as a pressure sensor for the real-time detection of **a** pulse, **b** phone vibration, **c** speaking, **d** smiling, **e** middle finger bending, and **f** knee bending. **g** Structure diagram of the array. **h** Resistance

changes of sugar cubes at different positions in the array. **i** Resistance changes of sugar cubes at different positions and weights in the array.

change rate under the pressure of a sugar cube in the front row was 15%, and the resistance change rate of two sugar cubes in the back row was 40%, which not only maintains high stability but also presents accurate recognition ability. Therefore, the strain sensor array based on AFGA-2 demonstrates its potential application in wearable pressure devices.

Conclusions

In this work, an ultralight pure graphene aerogel of AFGA with excellent mechanical properties was prepared using alkali to induce the arrangement of GO nanosheets and reductant of FAS to reduce GO, which has great application potential in the sensing field. The fabricated sensor based on AFGA can be

used for personal health monitoring, and a series of signals can be detected, including pulse, mobile phone vibration, smiling, talking, walking, finger bending, etc. At the same time, AFGA-based array sensors can also be assembled to detect pressure distribution, further expanding its application range. In summary, a simple and feasible strategy is applied to prepare a high-performance pure GA only using GO, which can further explore the sensor application of aerogels.

Acknowledgements

This work was funded by the National Natural Science Foundation of China (No. 51975562) and the

National Basic Research Program of China (JCKY2019130C105).

Declarations

Conflict of interest The authors declare no competing financial interest.

Supplementary Information: The online version contains supplementary material available at <http://doi.org/10.1007/s10853-022-08113-8>.

References

- [1] Souri H, Banerjee H, Jusufi A, Radacsi N, Stokes AA, Park I, Sitti M, Amjadi M (2020) Wearable and stretchable strain sensors: materials, sensing mechanisms, and applications. *Adv Intell Syst* 2:2000039. <https://doi.org/10.1002/aisy.202000039>
- [2] Gao S, Zhao X, Fu Q, Zhang T, Zhu J, Hou F, Ni J, Zhu C et al (2022) Highly transmitted silver nanowires-SWCNTs conductive flexible film by nested density structure and aluminum-doped zinc oxide capping layer for flexible amorphous silicon solar cells. *J Mater Sci Technol* 126:152–160. <https://doi.org/10.1016/j.jmst.2022.03.012>
- [3] Ji X, Zhong Y, Li C, Chu J, Wang H, Xing Z, Niu T, Zhang Z et al (2021) Nanoporous carbon aerogels for laser-printed wearable sensors. *ACS Appl Nano Mater* 4:6796–6804. <https://doi.org/10.1021/acsnm.1c00858>
- [4] He Y, Zhou M, Mahmoud MHH, Lu X, He G, Zhang L, Huang M, Elnaggar AY et al (2022) Multifunctional wearable strain/pressure sensor based on conductive carbon nanotubes/silk nonwoven fabric with high durability and low detection limit. *Adv Compos Hybrid Mater* 5:1939–1950. <https://doi.org/10.1007/s42114-022-00525-z>
- [5] Das HS, Roymahapatra G, Nabdu PK, Das R (2021) Study the effect of ZnO/Cu/ZnO multilayer structure by RF magnetron sputtering for flexible display applications. *ES Energy Environ* 13:50–56. <https://doi.org/10.30919/eseec8c441>
- [6] Kong D, El-Bahy ZM, Algadi H, Li T, El-Bahy SM, Nassan MA, Li J, Faheim AA et al (2022) Highly sensitive strain sensors with wide operation range from strong MXene-composited polyvinyl alcohol/sodium carboxymethylcellulose double network hydrogel. *Adv Compos Hybrid Mater* 5:1976–1987. <https://doi.org/10.1007/s42114-022-00531-1>
- [7] Hui Y, Xie W & Gu H (2021) Reduced Graphene Oxide/nanocellulose/amino-multiwalled carbon nanotubes nanocomposite aerogel for excellent oil adsorption. *ES Food Agroforestry* 5:38–44. <https://doi.org/10.30919/esfaf531>
- [8] Xiong S, Yang Y, Zhang S, Xiao Y, Ji H, Yang Z, Ding F (2021) Nanoporous polybenzoxazine aerogels for thermally insulating and self-extinguishing materials in aerospace applications. *ACS Appl Nano Mater* 4:7280–7288. <https://doi.org/10.1021/acsnm.1c01253>
- [9] Pan D, Yang G, Abo-Dief HM, Dong J, Su F, Liu C, Li Y, Xu BB et al (2022) Vertically aligned silicon carbide nanowires/boron nitride cellulose aerogel networks enhanced thermal conductivity and electromagnetic absorbing of epoxy composites. *Nano-Micro Lett* 14:118. <https://doi.org/10.1007/s40820-022-00863-z>
- [10] Wei D, Weng M, Mahmoud MHH, Elnaggar AY, Azab IHE, Sheng X, Huang M, El-Bahy ZM et al (2022) Development of novel biomass hybrid aerogel supported composite phase change materials with improved light-thermal conversion and thermal energy storage capacity. *Adv Compos Hybrid Mater* 5:1910–1921. <https://doi.org/10.1007/s42114-022-00519-x>
- [11] Dang C, Mu Q, Xie X, Sun X, Yang X, Zhang Y, Maganti S, Huang M et al (2022) Recent progress in cathode catalyst for nonaqueous lithium oxygen batteries: a review. *Adv Compos Hybrid Mater* 5:606–626. <https://doi.org/10.1007/s42114-022-00500-8>
- [12] Wu X, Hou K, Huang J, Wang J, Yang S (2018) Graphene-based cellular materials with extremely low density and high pressure sensitivity based on self-assembled graphene oxide liquid crystals. *J Mater Chem C* 6:8717–8725. <https://doi.org/10.1039/C8TC01853G>
- [13] Guo F, Jiang Y, Xu Z, Xiao Y, Fang B, Liu Y, Gao W, Zhao P et al (2018) Highly stretchable carbon aerogels. *Nat Commun* 9:881. <https://doi.org/10.1038/s41467-018-03268-y>
- [14] Pang K, Song X, Xu Z, Liu X, Liu Y, Zhong L, Peng Y, Wang J et al (2020) Hydroplastic foaming of graphene aerogels and artificially intelligent tactile sensors. *Sci Adv* 6, eabd4045. <https://doi.org/10.1126/sciadv.abd4045>
- [15] Lv Z, Liu J, Yang X, Fan D, Cao J, Luo Y, Zhang X (2020) Naturally derived wearable strain sensors with enhanced mechanical properties and high sensitivity. *ACS Appl Mater Interfaces* 12:22163–22169. <https://doi.org/10.1021/acami.0c04341>
- [16] Wu X, Han Y, Zhang X, Zhou Z, Lu C (2016) Large-area compliant, low-cost, and versatile pressure-sensing platform based on microcrack-designed carbon black@polyurethane sponge for human-machine interfacing. *Adv Funct Mater* 26:6246–6256. <https://doi.org/10.1002/adfm.201601995>
- [17] Zu G, Kanamori K, Nakanishi K, Lu X, Yu K, Huang J, Sugimura H (2019) Superelastic multifunctional aminosilane-crosslinked graphene aerogels for high thermal insulation, three-component separation, and strain/pressure-

- sensing arrays. *ACS Appl Mater Interfaces* 11:43533–43542. <https://doi.org/10.1021/acsami.9b16746>
- [18] Xie W, Yao F, Gu H, Du A, Lei Q, Naik N, Guo Z (2022) Magnetoresistive and piezoresistive polyaniline nanoarrays in-situ polymerized surrounding magnetic graphene aerogel. *Adv Compos Hybrid Mater* 5:1003–1016. <https://doi.org/10.1007/s42114-021-00413-y>
- [19] Lv L, Zhang P, Xu T, Qu L (2017) Ultrasensitive pressure sensor based on an ultralight sparkling graphene block. *ACS Appl Mater Interfaces* 9:22885–22892. <https://doi.org/10.1021/acsami.7b07153>
- [20] Lv W, Zhang C, Li Z, Yang Q-H (2015) Self-assembled 3D graphene monolith from solution. *J Phys Chem Lett* 6:658–668. <https://doi.org/10.1021/jz502655m>
- [21] Bai H, Chen Y, Delattre B, Tomsia Antoni P & Ritchie Robert O (Bioinspired large-scale aligned porous materials assembled with dual temperature gradients. *Sci Adv* 1: e1500849. <https://doi.org/10.1126/sciadv.1500849>
- [22] Hu H, Zhao Z, Wan W, Gogotsi Y, Qiu J (2013) Ultralight and highly compressible graphene aerogels. *Adv Mater* 25:2219–2223. <https://doi.org/10.1002/adma.201204530>
- [23] Wang L, Zhang M, Yang B, Tan J, Ding X (2020) Highly compressible, thermally stable, light-weight, and robust aramid nanofibers/Ti3AlC2 MXene composite aerogel for sensitive pressure sensor. *ACS Nano* 14:10633–10647. <https://doi.org/10.1021/acs.nano.0c04888>
- [24] Goldstein AP, Mickelson W, Machness A, Lee G, Worsley MA, Woo L, Zettl A (2014) Simultaneous sheet cross-linking and deoxygenation in the graphene oxide sol-gel transition. *J Phys Chem C* 118:28855–28860. <https://doi.org/10.1021/jp5092027>
- [25] Chen T, Wang J, Wu X, Li Z & Yang S (2021) Ethanedi-amine induced self-assembly of long-range ordered GO/MXene composite aerogel and its piezoresistive sensing performances. *Appl Surf Sci* 566:150719. <https://doi.org/10.1016/j.apsusc.2021.150719>
- [26] Xu X, Zhang Q, Yu Y, Chen W, Hu H, Li H (2016) Naturally dried graphene aerogels with superelasticity and tunable Poisson's ratio. *Adv Mater* 28:9223–9230. <https://doi.org/10.1002/adma.201603079>
- [27] Zhang X, Zhang T, Wang Z, Ren Z, Yan S, Duan Y, Zhang J (2019) Ultralight, superelastic, and fatigue-resistant graphene aerogel templated by graphene oxide liquid crystal stabilized air bubbles. *ACS Appl Mater Interfaces* 11:1303–1310. <https://doi.org/10.1021/acsami.8b18606>
- [28] Zhang J, Yang H, Shen G, Cheng P, Zhang J, Guo S (2010) Reduction of graphene oxide vial-ascorbic acid. *Chem Commun* 46:1112–1114. <https://doi.org/10.1039/B917705A>
- [29] Chua CK, Pumera M (2014) Chemical reduction of graphene oxide: a synthetic chemistry viewpoint. *Chem Soc Rev* 43:291–312. <https://doi.org/10.1039/C3CS60303B>
- [30] Chen W, Yan L (2011) In situ self-assembly of mild chemical reduction graphene for three-dimensional architectures. *Nanoscale* 3:3132–3137. <https://doi.org/10.1039/C1NR10355E>
- [31] Yao B, Chen J, Huang L, Zhou Q, Shi G (2016) Base-induced liquid crystals of graphene oxide for preparing elastic graphene foams with long-range ordered microstructures. *Adv Mater* 28:1623–1629. <https://doi.org/10.1002/adma.201504594>
- [32] Yang G, Yang Y, Chen T, Wang J, Ma L, Yang S (2022) Graphene/MXene composite aerogels reinforced by polyimide for pressure sensing. *ACS Appl Nano Mater* 5:1068–1077. <https://doi.org/10.1021/acsanm.1c03722>
- [33] Moon IK, Lee J, Ruoff RS, Lee H (2010) Reduced graphene oxide by chemical graphitization. *Nat Commun* 1:73. <https://doi.org/10.1038/ncomms1067>
- [34] Yu H, Wang B, Zhou S, Zhu M, Chen W, Chen H, Li X, Liang S et al (2021) Polyvinylpyrrolidone functionalization induces deformable structure of graphene oxide nanosheets for lung-targeting delivery. *Nano Today* 38: 101151. <https://doi.org/10.1016/j.nantod.2021.101151>
- [35] Yang H, Zhang T, Jiang M, Duan Y, Zhang J (2015) Ambient pressure dried graphene aerogels with superelasticity and multifunctionality. *J Mater Chem A* 3:19268–19272. <https://doi.org/10.1039/C5TA06452J>
- [36] Wicklein B, Kocjan A, Salazar-Alvarez G, Carosio F, Camino G, Antonietti M, Bergström L (2015) Thermally insulating and fire-retardant lightweight anisotropic foams based on nanocellulose and graphene oxide. *Nat Nanotechnol* 10:277–283. <https://doi.org/10.1038/nnano.2014.248>
- [37] Phan C M (2021) The surface tension and interfacial composition of water/ethanol mixture. *J Mol Liq* 342: 117505. <https://doi.org/10.1016/j.molliq.2021.117505>
- [38] Wang C, He X, Shang Y, Peng Q, Qin Y, Shi E, Yang Y, Wu S et al (2014) Multifunctional graphene sheet–nanoribbon hybrid aerogels. *J Mater Chem A* 2:14994–15000. <https://doi.org/10.1039/C4TA02591A>
- [39] Yang W, Peng D, Kimura H, Zhang X, Sun X, Pashameah RA, Alzahrani E, Wang B et al (2022) Honeycomb-like nitrogen-doped porous carbon decorated with Co3O4 nanoparticles for superior electrochemical performance pseudo-capacitive lithium storage and supercapacitors. *Adv Compos Hybrid Mater*. <https://doi.org/10.1007/s42114-022-00556-6>
- [40] Meyer JC, Geim AK, Katsnelson MI, Novoselov KS, Booth TJ, Roth S (2007) The structure of suspended graphene

- sheets. *Nature* 446:60–63. <https://doi.org/10.1038/nature05545>
- [41] Bai S, Shen X, Zhu G, Yuan A, Zhang J, Ji Z, Qiu D (2013) The influence of wrinkling in reduced graphene oxide on their adsorption and catalytic properties. *Carbon* 60:157–168. <https://doi.org/10.1016/j.carbon.2013.04.009>
- [42] Chen P-Y, Sodhi J, Qiu Y, Valentin TM, Steinberg RS, Wang Z, Hurt RH, Wong IY (2016) Multiscale graphene topographies programmed by sequential mechanical deformation. *Adv Mater* 28:3564–3571. <https://doi.org/10.1002/adma.201506194>
- [43] Hu K-M, Liu Y-Q, Zhou L-W, Xue Z-Y, Peng B, Yan H, Di Z-F, Jiang X-S et al (2020) Delamination-free functional graphene surface by multiscale, conformal wrinkling. *Adv Funct Mater* 30:2003273. <https://doi.org/10.1002/adfm.202003273>
- [44] Fan Z-J, Kai W, Yan J, Wei T, Zhi L-J, Feng J, Ren Y-M, Song L-P et al (2011) Facile synthesis of graphene nanosheets via Fe reduction of exfoliated graphite oxide. *ACS Nano* 5:191–198. <https://doi.org/10.1021/nn102339t>
- [45] Kuila T, Bose S, Khanra P, Mishra AK, Kim NH, Lee JH (2012) A green approach for the reduction of graphene oxide by wild carrot root. *Carbon* 50:914–921. <https://doi.org/10.1016/j.carbon.2011.09.053>
- [46] Ma Q, Song J, Jin C, Li Z, Liu J, Meng S, Zhao J, Guo Y (2013) A rapid and easy approach for the reduction of graphene oxide by formamidesulfonic acid. *Carbon* 54:36–41. <https://doi.org/10.1016/j.carbon.2012.10.067>
- [47] Chua CK, Ambrosi A, Pumera M (2012) Graphene oxide reduction by standard industrial reducing agent: thiourea dioxide. *J Mater Chem* 22:11054–11061. <https://doi.org/10.1039/C2JM16054D>
- [48] Liu H, Chen X, Zheng Y, Zhang D, Zhao Y, Wang C, Pan C, Liu C et al (2021) Lightweight, superelastic, and hydrophobic polyimide nanofiber /MXene composite aerogel for wearable piezoresistive sensor and oil/water separation applications. *Adv Funct Mater* 31:2008006. <https://doi.org/10.1002/adfm.202008006>
- [49] Ma Y, Yue Y, Zhang H, Cheng F, Zhao W, Rao J, Luo S, Wang J et al (2018) 3D synergistical MXene/reduced graphene oxide aerogel for a piezoresistive sensor. *ACS Nano* 12:3209–3216. <https://doi.org/10.1021/acsnano.7b06909>

Publisher's Note Springer Nature remains neutral with regard to jurisdictional claims in published maps and institutional affiliations.

Springer Nature or its licensor (e.g. a society or other partner) holds exclusive rights to this article under a publishing agreement with the author(s) or other rightsholder(s); author self-archiving of the accepted manuscript version of this article is solely governed by the terms of such publishing agreement and applicable law.